ARTICLE

fib WILEY

Influence of specimen size on the fibre geometry and tensile strength of ultra-high-performance fibre-reinforced concrete

Kasem Maryamh[1] | **Konstantin Hauch[2]** | **Claudia Redenbach[2]** | **Jürgen Schnell[1]**

[1]Faculty of Civil Engineering, Technische Universität Kaiserslautern, Institute of Concrete Structures and Structural Design, Kaiserslautern, Germany

[2]Department of Mathematics, Technische Universität Kaiserslautern, Kaiserslautern, Germany

Correspondence
Kasem Maryamh, Faculty of Civil Engineering, Technische Universität Kaiserslautern, Institute of Concrete Structures and Structural Design, Paul-Ehrlich-Straße 14, D-67663 Kaiserslautern, Germany.
Email: kasem.maryamh@bauing.uni-kl.de

Funding information
Deutsche Forschungsgemeinschaft, Grant/Award Number: RTG 1932

Abstract

The influence of the specimen size of ultra-high-performance fibre-reinforced concrete samples on the spatial distribution and orientation of the steel fibres is investigated. Specimens of varying size are produced by using the same protocol. They are imaged by micro-computed tomography to perform a statistical analysis of the spatial arrangement of the fibres. The tensile strength of the specimens is measured by tensile tests on subspecimens of equal size. The results are correlated to geometric characteristics of the fibre systems determined from the image data. Increasing the specimen size results in a larger variability of the local fibre geometry. This effect was most prominent when increasing the height of the specimens.

KEYWORDS
fibre geometry, size effect, UHPFRC, uniaxial tensile strength

1 | INTRODUCTION

Building complex and sophisticated structures demands an innovative solution to reinforce both large and filigree elements. Large elements bear strong shrinkage and mostly need a huge amount of rebars. These may aggravate the casting process which causes air voids in the elements. In contrast, filigree elements have no space to place suitable rebars. In such situations, ultra-high-performance fibre-reinforced concrete (UHPFRC) yields a promising alternative. Fibre reinforcement does not only stand out as a good solution to reduce rebars and shrinkage impacts but fibre reinforced concretes can be considered integrated materials rendering conventional reinforcement dispensable.

It is well-known that adding steel fibres to UHPC is essential to increase the ductility of the composite material.[1–5] Mechanical properties of UHPFRC under loading depend decisively on the fibre geometry, that is, the local fibre content and the fibre orientation.[6] In general, the orientation and distribution of the fibres (fibre geometry) in fibre reinforced concrete show an anisotropic behaviour. In self-compacting concrete, the fibre geometry is

---

mainly influenced by the flow direction where the fibres primarily align. Fibres aligned along the tension axis considerably contribute to the tensile strength.[7] Therefore, if possible, the flow direction during production should be aligned to the tensile axis. However, the influence of the flow field should be considered.[8] A review of the influence of steel fibres on the compressive and tensile strength of UHPFRC can be found in Reference 9. The authors summarise the results of 37 publications dealing with the evaluation of compressive or tensile strength of fibre reinforced concrete. In these studies, the influence of the concrete mixture and of parameters such as the fibre content, fibre shape and size on the mechanical behaviour of concrete specimens was thoroughly investigated. The typical design considers fibre volume fractions in the range of 0 to 3%. Different fibre shapes are used, the most frequent one being straight fibres with a length of 12–13 mm and a diameter of 0.2 mm. Typical specimen shapes used for compression tests are cubes with an edge length ranging from 40 to 150 mm or cylinders with a diameter ranging from 50 to 100 mm and a length between 150 and 300 mm. For bending tests, prisms in the size range $40 \times 40 \times 160$ mm^3 to $100 \times 100 \times 400$ mm^3 are common while dog bone shapes are preferred for tensile tests. In most studies, specimen size and shape were constant. As a consequence, the influence of these parameters, henceforth termed size effect, on the mechanical concrete behaviour is less well understood.[9–12]

Experimental results investigating the effect of specimen size in compression or bending tests are reported in Reference 10–14. In these studies, a decrease of flexural strength for increasing sample size is reported. Attempts to explain this finding include both a statistical and a deterministic approach.[11,13] The statistical approach according to Weibull's theory[15] basically states that larger specimens are more likely to contain severe flaws or defects that reduce the strength of the specimen. The deterministic effect is based on the fact that deformation is concentrated in a localisation band whose size depends on the maximum aggregate size in concrete. In small specimens, the size of this zone is significant compared to the specimen size while it is negligible in reasonably large specimens. This effect is considered in Bažant's theory which is based on fracture mechanics.[16,17] An additional effect that is still poorly acknowledged is that a change of specimen dimensions may also result in local variations in fibre geometry. In particular, the degree of edge effects due to the interaction of the fibres with the edges of the formwork or sedimentation of fibres may differ when producing specimens of different size.

A first publication investigating this effect is.[14] The authors study the size effect on the flexural performance of UHPFRC by using three different specimen sizes. Distribution and orientation of fibres in the specimens were investigated by image analysis of two-dimensional cross-sections at the crack surfaces. The investigation revealed that the flexural performance noticeably decreases with an increase in the specimen size resulting from an inhomogeneous spatial fibre distribution and a poor fibre alignment along the tension axis. For specimens of different size but with comparable fibre distribution properties, an insignificant size effect on the flexural strength was observed for UHPC with 2% steel fibre volume fraction.

In this article, we aim at a characterisation of size effects in the local fibre geometry in UHPFRC specimens in a fully three-dimensional manner. To this end, specimens produced as prisms of different size are studied by using micro-computed tomography (μCT) imaging. In a prior study,[6] local fibre content and fibre orientation were studied for concrete with differing mix consistency, fibre thickness, fibre content and casting point. Here, the parameter combination resulting in the concrete with the highest flexural strength was selected to produce concrete beams of varying size. Using the geometric characteristics established in,[6] the fibre systems were characterised locally and the results were correlated to the tensile strength of the specimens.

2 | EXPERIMENTAL PROGRAM

2.1 | Production of the UHPFRC-specimens

In the prior study,[6] the rheology of UHPC-mixtures with a maximum grain size of 1 mm was modified by varying the amount of superplasticizer in the mixture. As the mixture M02 with an intermediate amount of superplasticizer resulted in the most promising fibre geometries, the same mixture is used here.[6] Details on the constituents and specifications can be found in Table 1. Concrete was produced by using the Eirich-Intensive

TABLE 1 Constituents, bending tensile strength and compression strength of the UHPC-mixture M02

Cement CEM I 52.5 R SR3-NA (Sulfo 5R)	825 g/L
Quarz Sand 0.125/0.5 Haltern	975 g/L
Quarz Flour-MILLISIL-W12	200 g/L
Silica fume: Sika Silicoll P uncompacted	175 g/L
Water	179 g/L
PCE-plasticizer—Sika Viscocrete 2810	30.25 g/L
Bending tensile strength	13.77 MPa
Compression strength	150.2 MPa

Vacuum mixer of 70 L volume capacity. The same procedure and mix regime as given in Reference 6 were applied. For reinforcement, fibres with an ultimate tensile strength of 2.800 MPa and elasticity modulus of 200.000 MPa were used. The fibre volume fraction was 2%, and the fibre aspect ratio was lf/df = 12.5/0.2 mm. The fresh concrete tests showed similar spread flow, bulk density and void content values as reported in Reference 6. The casting of the specimens was carried out from the side, reproducing the configuration M02F2s02 from Reference 6. Five sizes of specimens were produced: $40 \times 40 \times 160$ mm^3 (denoted by $4 \times 4 \times 16$), $80 \times 40 \times 160$ mm^3 (denoted by $8 \times 4 \times 16$), $40 \times 40 \times 320$ mm^3 (denoted by $4 \times 4 \times 32$), $40 \times 80 \times 320$ mm^3 (denoted by $4 \times 8 \times 32$) and $80 \times 80 \times 320$ mm^3 (denoted by $8 \times 8 \times 32$). To ensure the uniformity of the concrete flow over the different widths of the specimens, a chute with an adjustable casting width (Figure 1) was designed and produced at the lab of the Department of Concrete Structures and Structural Design, University of Kaiserslautern, Germany. The chute enables a variation of the casting width from 4 up to 15 cm with nearly similar flow velocity.

The specimens were cured in a climate chamber for 28 days. Since the maximal specimen size for computed tomography imaging is $40 \times 40 \times 160$ mm^3, the larger specimens were sawn into subvolumes of this size. Water jet technology with a beam width of approximately 1 mm was used to cut the specimens. This method causes nearly no microcracks in the specimens compared to the conventional sawing method. Figure 2 shows the specimens after cutting.

2.2 | Micro-computed tomography imaging

The specimens were scanned by micro-computed tomography (μCT) at the Fraunhofer Institut für Techno-und Wirtschaftsmathematik (ITWM) in Kaiserslautern, Germany.
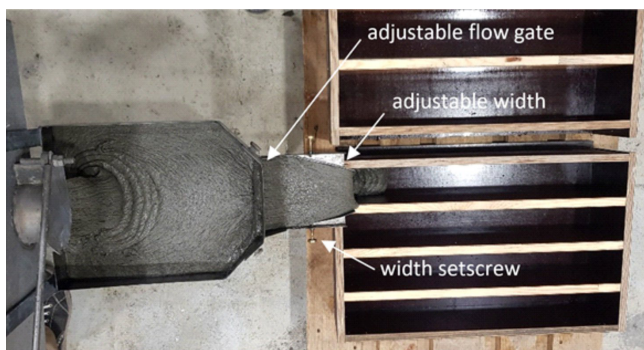
To reduce grey value variations in the images, the prismatic specimens were placed in a cylindrical UHPC shell during the scanning process. Table 2 summarises the CT specifications and imaging parameters. A specimen of size $40 \times 40 \times 160$ mm^3 corresponds to a reconstructed image of $441 \times 441 \times 1766$ pixels. Figure 3 shows a visualisation of one specimen together with the coordinate system used for the analysis: depth, height and length of the specimen correspond to the X, Y and Z coordinate axis, respectively. The plane $Y = 0$ mm represents the bottom of the sample. The casting point is located at $Z = 0$ mm, $X = 20$ mm (40 mm) for depth 40 mm (80 mm) and $Y = 40$ or 80 mm corresponding to the top of the specimens. The flow direction of the UHPFRC was along the Z-coordinate direction.

2.3 | Tensile tests

As the specimens had to be cut for the CT imaging, testing the flexural strength of the complete specimens was
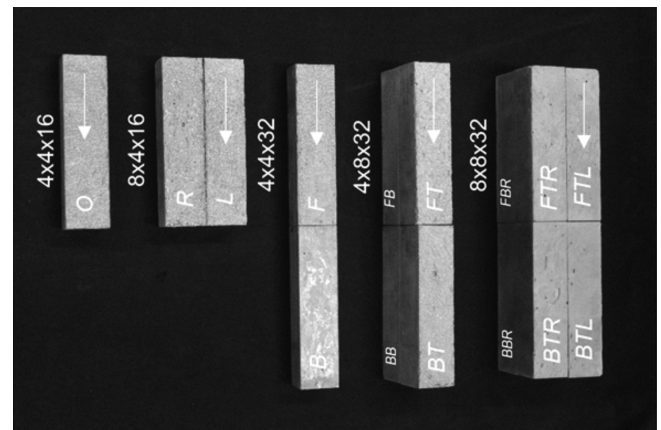

FIGURE 2 The sawed specimens with the notation of the subspecimens according to position: O: original specimen size, R: right, L: left, F: front, B: back, T: top and B: bottom. Arrows indicate the casting direction

FIGURE 1 Production of the specimens using a chute with adjustable casting width

TABLE 2 CT specifications and imaging parameters

CT tube	Feinfocus FXE 225.51
Maximum acceleration	225 kV
Maximum power	20 W
Detector	Perkin Elmer XRD 1621
Detector size	2048×2048 pixels
Tube voltage	190 kV
Target electricity	65 μA
Applied power	12 W
No. of projections	800
Voxel edge length	90.6 μm

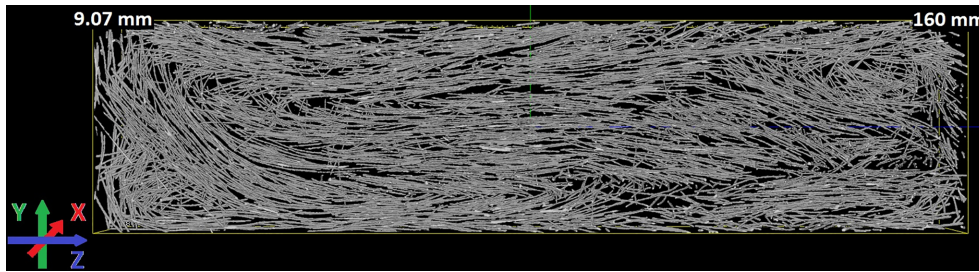**FIGURE 3** 3D coordinate system and fibre system reconstruction of a subvolume of specimen 4 × 4 × 16. The visualised volume corresponds to 100 × 441 × 1766 pixels
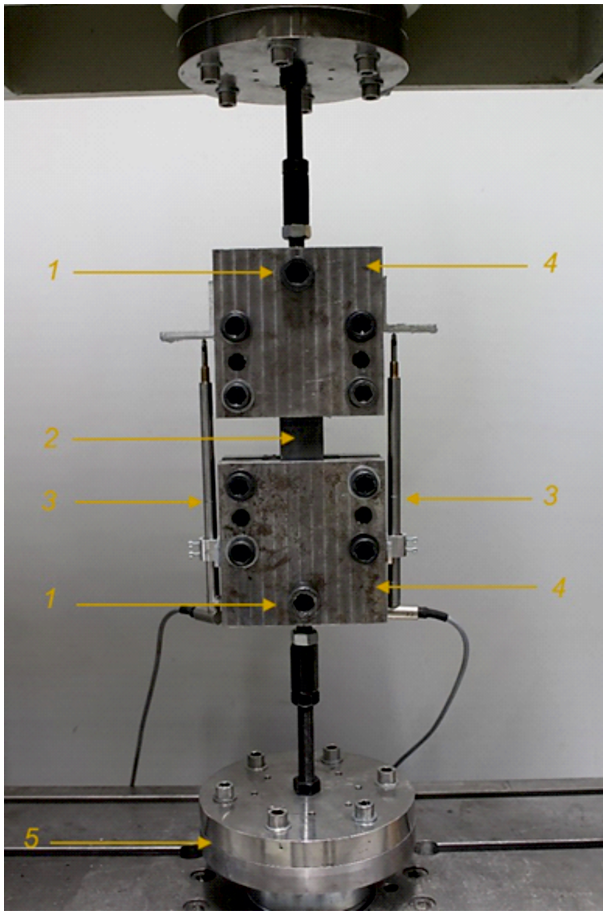

FIGURE 4 (1) Setup of the uniaxial tensile test: rotatable hinge, (2) specimen, (3) extensometer on both sides to measure the elongation, (4) griping jaw, and (5) load cell

no longer possible. To characterise the 17 subspecimens mechanically, uniaxial tensile tests were carried out to determine the tensile strength.

A challenge was to develop a test setup, which enables to apply a uniaxial tension on specimens of prism form, the main point being the fixation of the specimens at the ends. The test set up shown in Figure 4 provided a reasonable result regarding fixing rigidity and convenient handing. The specimen was placed in the gripping jaws with a contact area of 40 × 60 mm² and fixed by six bolts, which were pulled by a moment of 110 Nm. This pull

moment was determined as the maximum so that no cracks occur in the clamping area. After fixing both ends, the set was fixed in the pull machine by two nuts. In this set up, a field of length 40 mm located in the middle of the specimens was tensioned.

The tests were carried out in a displacement-controlled manner. A low load rate of 0.1 mm/min was chosen. The lengthening of the 40 mm field was measured by using two extensometers. The test was stopped as soon as the lengthening of the field reached 2 mm. During the uniaxial tensile tests, load-lengthening curves were recorded. Since the subspecimens have a small difference in the cross-section, the uniaxial stress–strain curves were determined to compare the results consistently. It was assumed that the stress distribution remains uniform over the cross-section through the first cracking phase and after the crack localisation, although it is well known that an eccentricity occurs in the internal resistance forces because of nonuniform distribution of the fibres in the cross-section. Based on this fact the calculated stress will be considered as equivalent uniaxial stress f. The strain ϵ is the measured lengthening ΔL divided by the tensioned length ($L = 40$ mm). That is,

$$f = \frac{F}{A} \text{ and } \in = \frac{\Delta L}{L}$$

where F is the force value and A is the area of the cross-section. Two strength values were computed for every specimen: the elastic post-crack tensile strength ($f_{cft,el}$), which corresponds to the force at the end of the linear phase in the curve (limit of proportionality) in sense of,[18] and the ultimate post-crack tensile strength ($f_{cft,ult}$) which corresponds to the maximum force reached.

3 | IMAGE ANALYSIS

3.1 | Image processing

For image processing, we used the software tools MAVI (Modular Algorithms for Volume Images)[19] and ToolIP (Tool for Image Processing).[20] The CT images contain
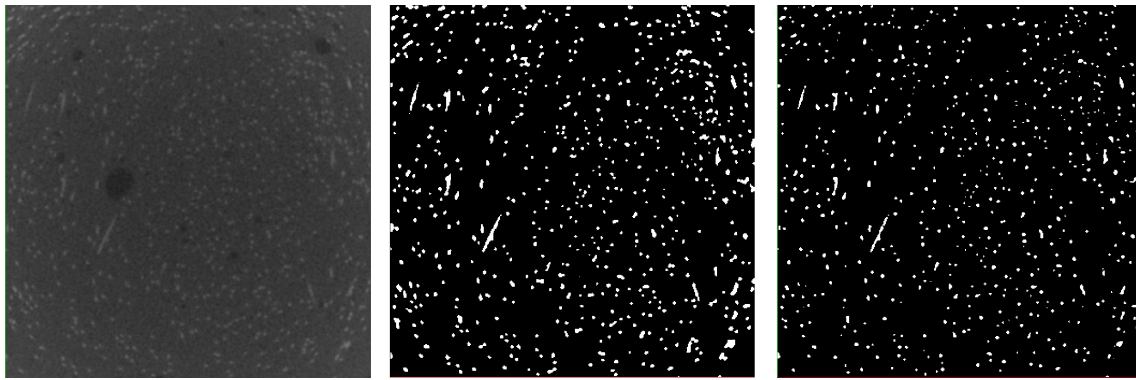
FIGURE 5 Left: Sectional image of a 3D image. Middle: Binarisation without removal of the illumination gradients resulting in over-segmentation in the edge areas. Right: Binarisation by using the procedure detailed in the text
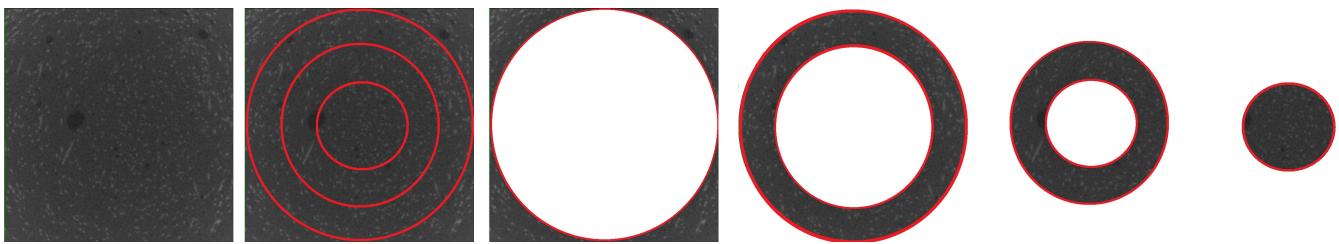

FIGURE 6 From left to right: The initial image, the cylindrical subdivision of the image and the single image parts after cropping

illumination gradients from the edges of the specimen to the centre.[21] Hence, an illumination correction was necessary to reconstruct the fibre system correctly, see Figure 5 for an illustration.

The following chain of image processing steps was applied:

1. Filtering of the initial image by a mean filter.[22] The size of the cubic filter mask is chosen such that the largest object (typically an air pore) in the initial image is covered.
2. Subtraction of the filtered image from the initial image.
3. Division of the image into cylinders whose bases form concentric rings/discs in the XY plane, see Figure 6.
4. Segmentation of the fibres in the image parts by using Otsu's method.[23]
5. Merging of the image parts.

The choice of subdivision was validated by checking whether the segmented fibres have a constant diameter throughout the image. This is done by comparing the values of local maxima of the Euclidean distance transform.[24]

Figure 7 shows a sectional image of specimen $4 \times 4 \times 16$ obtained by μCT and its binarisation. The subdivision shown in Figure 6 was used for all images in the study.

3.2 | Fibre content

We assessed the homogeneity of the fibre content along the coordinate directions. For this purpose, we computed area fraction profiles (AFP) which represent the area fraction of the fibres in each slice orthogonal to a coordinate direction. In macroscopically homogeneous microstructures, the expected area fraction in a 2D slice is equal to the volume fraction of the complete specimen.[25] Spatial inhomogeneities such as layer structures or varying fibre density lead to significant variations of the area fraction. The partial volume effect[26] in CT imaging and the low resolution of the images (2–3 pixels per fibre diameter) led to deviations between the estimated fibre volume fraction and the nominal value of 2%. To be able to compare the specimens with each other, the AFPs were centred. That is, the volume fraction of the complete specimen was subtracted from the area fractions in the slices. To compare the centred AFPs visually, the curves were smoothed by exponential smoothing with the parameter $\alpha = 0.05$ (R-function HoltWinters, R-packet statistics[27]), see Figure 8.
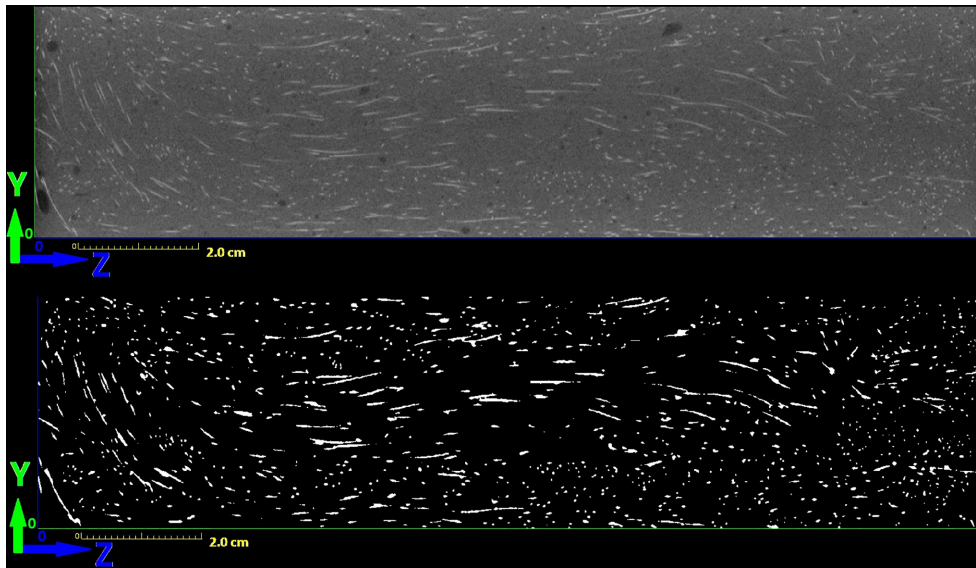
FIGURE 7 Top: Sectional μCT image of specimen $4 \times 4 \times 16$. Fibres are white, concrete matrix is grey, and air pores are black. Bottom: Binarisation of the fibre system
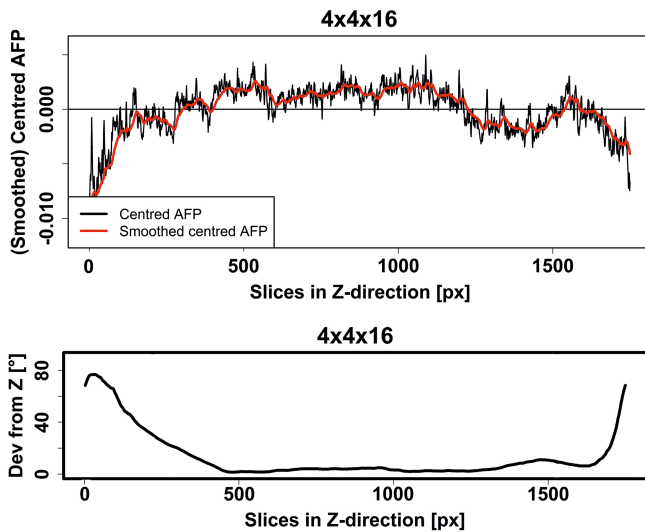

FIGURE 8 Top: Centred area fraction profile of specimen $4 \times 4 \times 16$ before (black) and after (red) smoothing. Bottom: Deviation (Dev) of the fibre orientation from the Z-axis (in degrees) in each slice of specimen $4 \times 4 \times 16$ along the Z-direction

3.3 | Fibre orientation

The local orientation of the fibres in the concrete was estimated based on partial second derivatives.[28,29] For this purpose, the initial image f is smoothed by applying an isotropic Gaussian convolution filter with kernel g_σ at scale σ to reduce noise in the grey values. For the resulting image, the Hessian matrix

$$H(f) = \begin{pmatrix} f_{xx} & f_{xy} & f_{xz} \\ f_{yx} & f_{yy} & f_{yz} \\ f_{zx} & f_{zy} & f_{zz} \end{pmatrix}$$

is computed, where

$$f_{ij} = \frac{\partial^2}{\partial i \partial j}(f * g_\sigma), \mathrm{i,j} \in \{x,y,z\}$$

are the second order derivatives of the smoothed image.

We follow the recommendation of Wirjadi et al.[29] and set σ equal to the fibre radius. For each fibre pixel p, the eigenvector corresponding to the smallest eigenvalue of $H(f)$ estimates the local fibre orientation in the point p. The fibre orientations (x_i, y_i, z_i) in a slice of the 3D image are averaged by using the orientation matrix.[30]

$$T = \begin{pmatrix} \sum_i x_i^2 & \sum_i x_i y_i & \sum x_i z_i \\ \sum_i x_i y_i & \sum_i y_i^2 & \sum_i y_i z_i \\ \sum_i x_i z_i & \sum_i y_i x_i & \sum_i z_i^2 \end{pmatrix}$$

The eigenvector of T with the largest eigenvalue represents the main fibre orientation within the slice. A fibre orientation along the Z-axis, that is, the tension axis, is desirable. Therefore, we compute the deviation of the main fibre orientation from the Z-axis (see Figure 8). As for the AFP, we smoothed the curves by exponential smoothing.

4 | RESULTS

In the following, we describe the results of tensile tests and the fibre geometry analysis of the individual specimens. Recall that the Z-axis of the coordinate system corresponds to the flow direction during casting and to the tensile axis in the tensile tests.

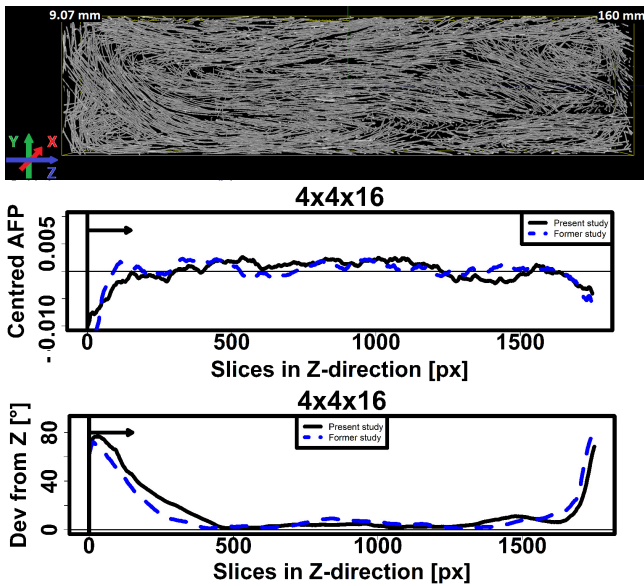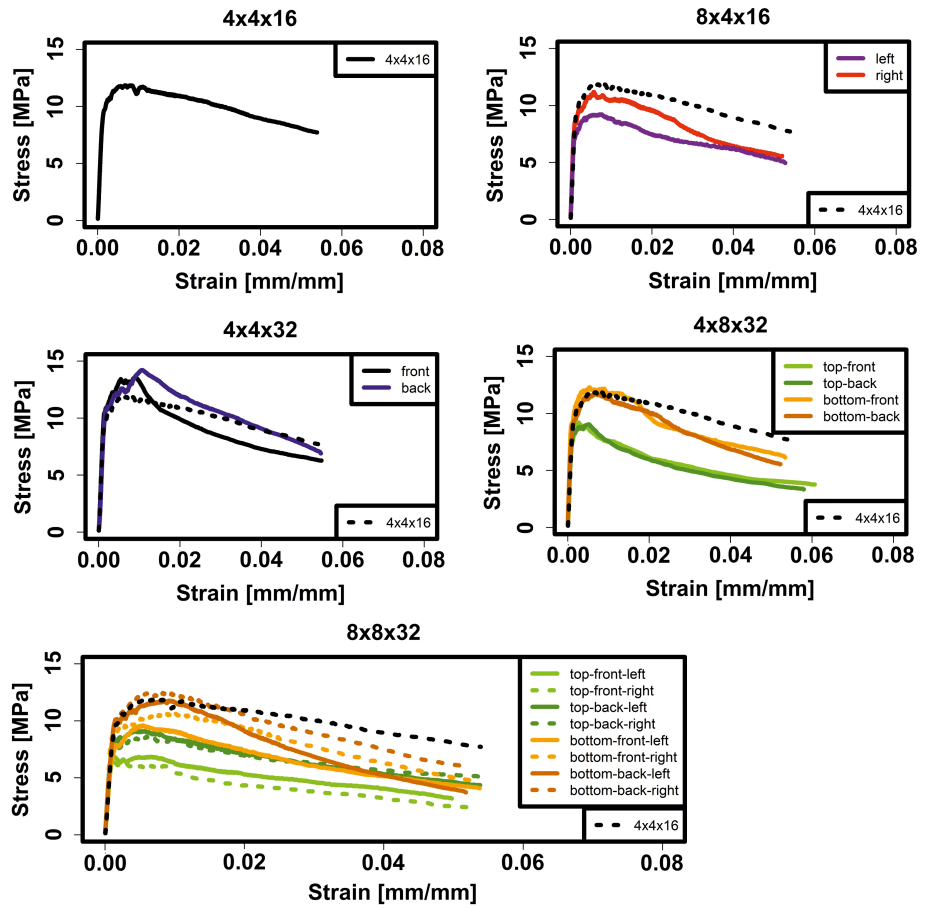**FIGURE 9** Stress–strain curves for all specimens

FIGURE 10 Specimen $4 \times 4 \times 16$: Subvolume rendering (top), centred AFP (middle), and deviation of the fibre orientations from the Z-axis (bottom) along the Z-direction. The curves obtained for specimen M02F2s02 in[6] are shown as dashed blue lines. The casting point is marked with a vertical line and the flow direction is illustrated by an arrow
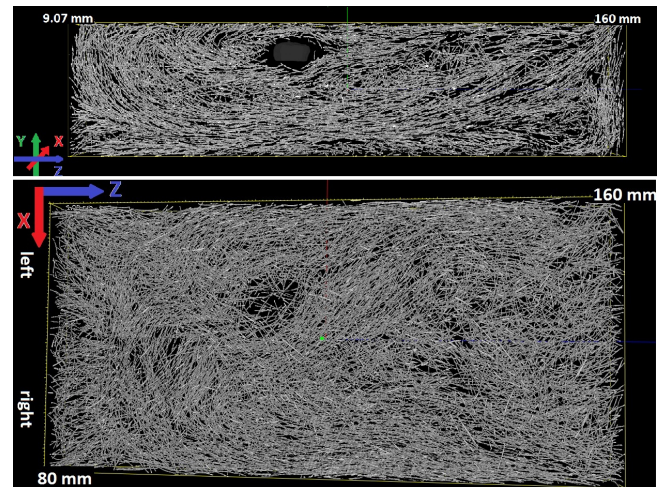
FIGURE 11 Silica agglomeration (dark grey) located in the upper left part of specimen $8 \times 4 \times 16$. Top: View from the side. Bottom: View from the top

Stress–strain curves are shown in Figure 9. In general, the tensile behaviour of all subspecimens looks similar and the initial stiffness is almost identical. It is mostly strain hardening behaviour with a very few exceptions.

However, there are obvious differences in tensile strength of the different subspecimens. In the following, each specimen will be discussed separately.

4.1 | Specimen 4 × 4 × 16

This specimen is of the same size as the specimens investigated in the prior study.[6] It mainly serves as a baseline and to ensure reproducibility of the production and the analysis protocols. Indeed, the plots for the AFP and the fibre

orientation deviation shown in Figure 10 are similar for the new specimen and the specimen used in Reference 6. The stress strain curve shown in Figure 9a cannot be compared to the prior study where bending, not tensile, tests were performed.

4.2 | Specimen 8 × 4 × 16

The stress strain curves of specimen 8 × 4 × 16 are shown in Figure 9b. Based on the production process,

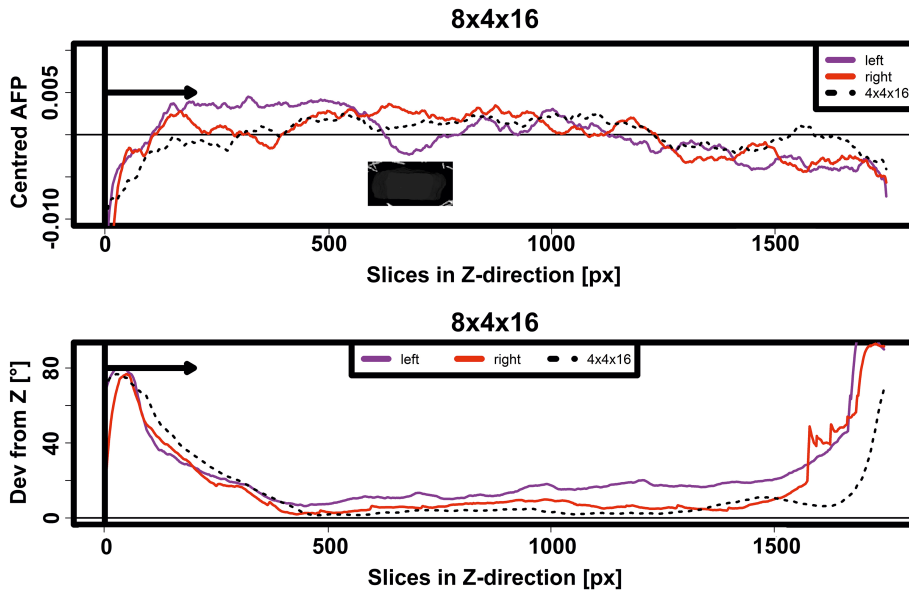**FIGURE 12** Specimen 8 × 4 × 16: Centred AFP along the Z-direction (top), and deviation of the fibre orientations from the Z-axis (bottom) along the Z-direction. The position of the silica fume agglomeration is shown in dark grey. The casting point is marked with a vertical line and the flow direction is illustrated by an arrow
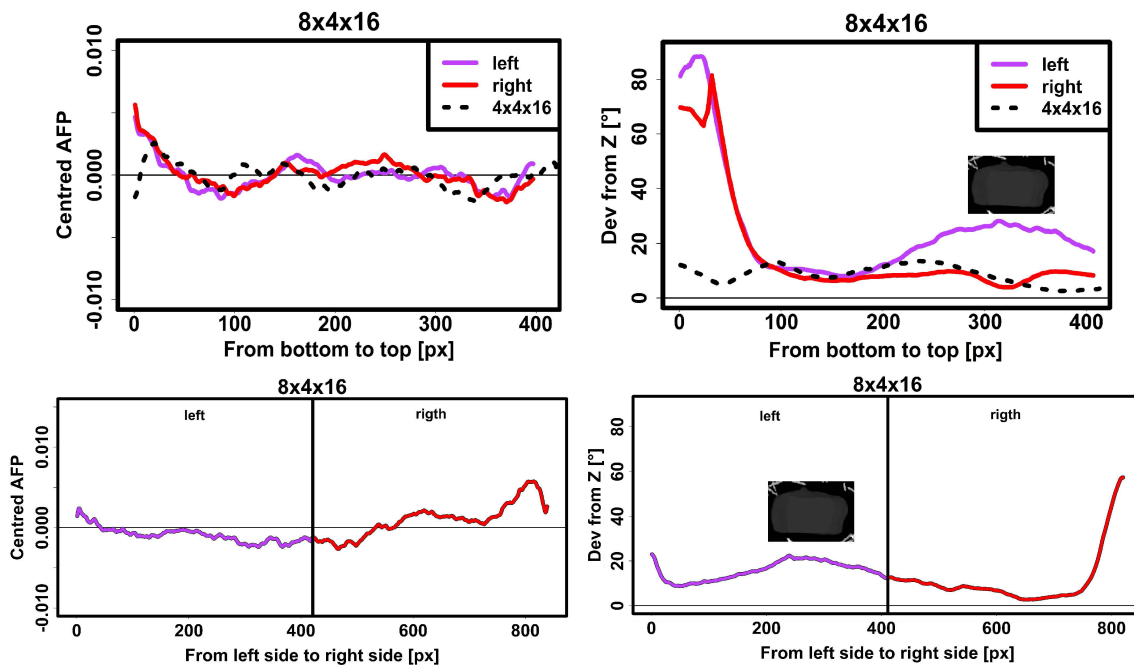

FIGURE 13 Specimen 8 × 4 × 16: Centred AFP (left) and deviation of the fibre orientations from the Z-axis (right) along Y-direction (top) and along the X-direction (bottom). The position of the silica agglomeration is shown in dark grey

similar results for the left and the right specimen are expected. The observation that the left specimen is weaker than the right one can be explained by the presence of a large agglomeration of silica fume in the left part of the specimen, see Figure 11.

Both specimen parts are slightly weaker than specimen $4 \times 4 \times 16$ which may be explained by a larger variability of the local fibre geometry. In particular, we observe slightly stronger fibre misalignment than in specimen
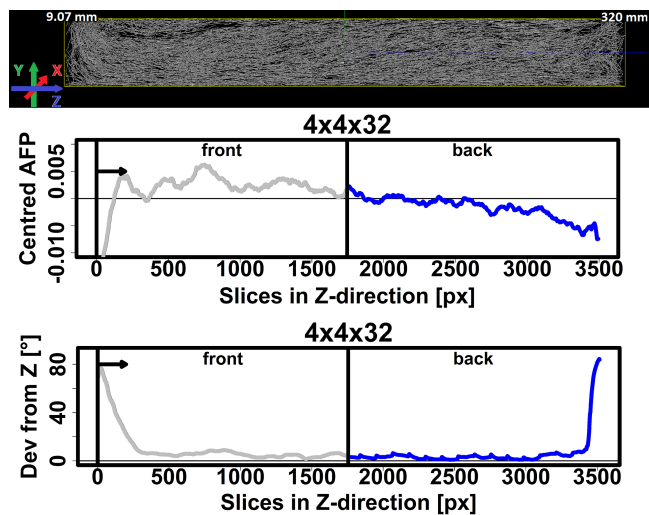
$4 \times 4 \times 16$, see Figure 12. Additionally, fibre misalignment is observed in the bottom part of the specimen, see Figure 13. Due to the increased specimen width, flow lines to the side are observed resulting in fibres pointing towards the outer edge of the samples in X-direction. The fibre content is reduced in the left specimen part which
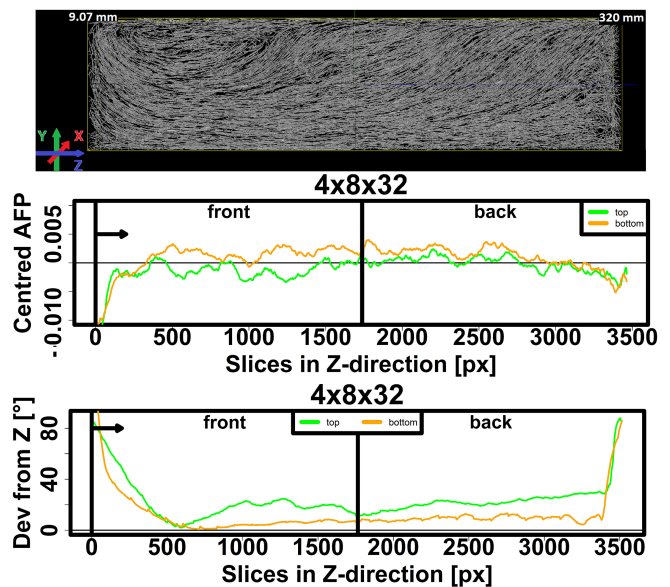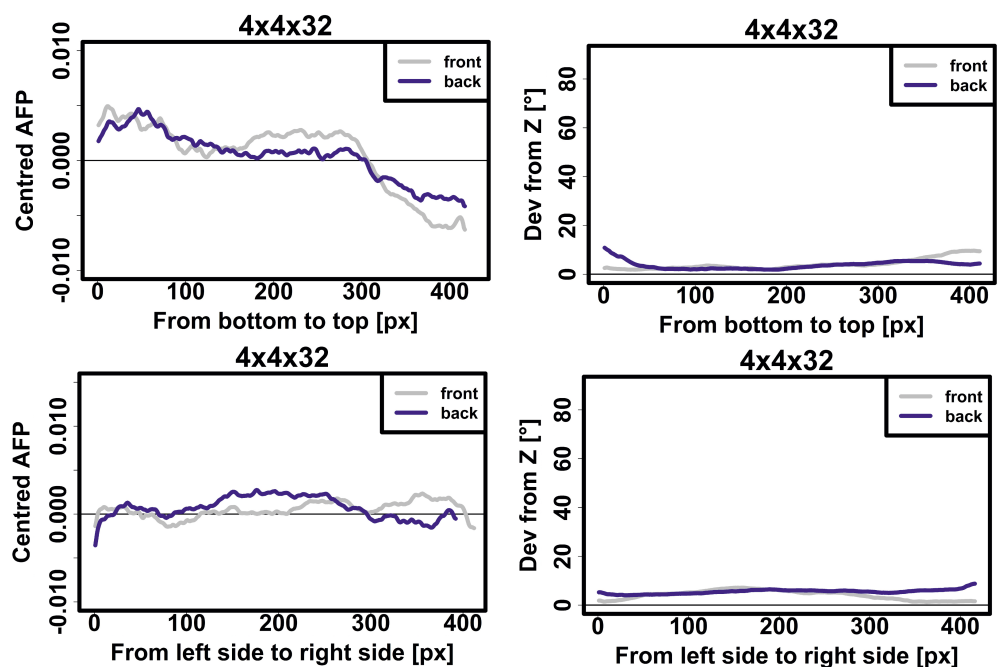

FIGURE 14 Specimen $4 \times 4 \times 32$: Subvolume rendering (top), centred AFP (middle) and deviation of the fibre orientations from the Z-axis (bottom) along the Z-direction. The casting point is marked with a vertical line and the flow direction is illustrated by an arrow

FIGURE 16 Specimen $4 \times 8 \times 32$: Subvolume rendering (top), centred AFP (middle) and deviation of the fibre orientations from the Z-axis (bottom) along the Z-direction. The casting point is marked with a vertical line and the flow direction is illustrated by an arrow. The subvolume rendering shows less fibres in the top front part of the specimen than in the bottom front part

FIGURE 15 Specimen $4 \times 4 \times 32$: Centred AFP (left) and deviation of the fibre orientations from the Z-axis (right) along Y-direction (top) and along the X-direction (bottom)

FIGURE 17 Specimen 4 × 8 × 32: Centred AFP (left) and deviation of the fibre orientations from the Z-axis (right) along Y-direction (top) and along the X-direction (bottom). 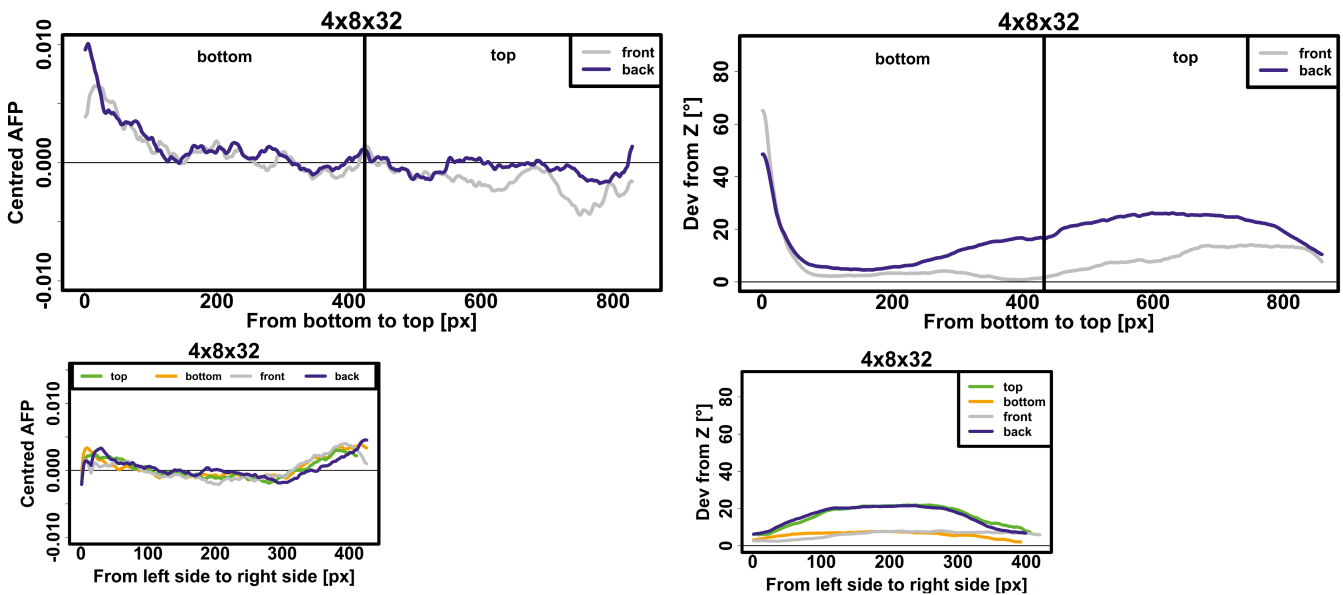Figure 18: Specimen 8 × 8 × 32: Subvolume rendering (top), centred AFP (middle) and deviation of the fibre orientations from the Z-axis (bottom) along the Z-direction. The casting point is marked by a vertical line and the flow direction is illustrated by an arrow

FIGURE 18 Specimen 8 × 8 × 32: Subvolume rendering (top), centred AFP (middle) and deviation of the fibre orientations from the Z-axis (bottom) along the Z-direction. The casting point is marked by a vertical line and the flow direction is illustrated by an arrow
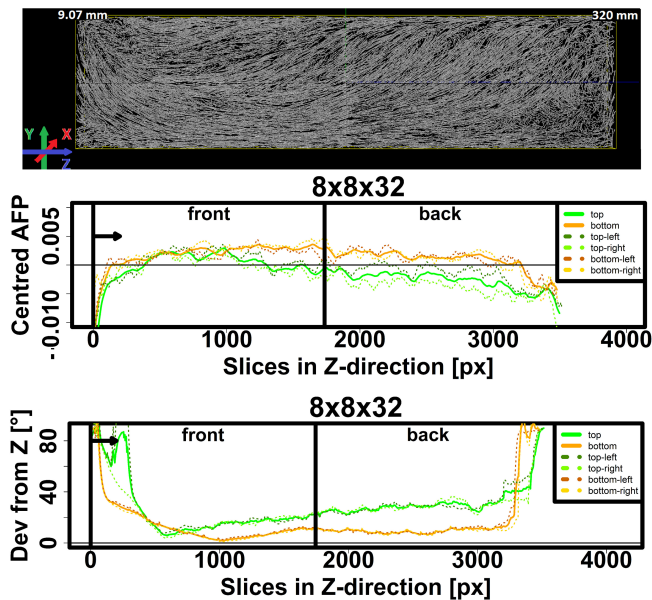
In the opinion of the authors, the increasing fibre fraction at the bottom (Figure 13, top left) should not be interpreted as fibre sedimentation. The consistency of the mixture is very stable and the fibre geometry shown in Figure 11 does not indicate fibre sedimentation. In contrast, the fibre geometry looks integrated, coherent and harmonious as expected for the given flow direction and casting point. The large deviation of the fibres from the Z-direction in the bottom part is probably caused by the interaction between the first concrete layers during the casting process, when the fibre concrete of the new layer flows over the previous one. This also applies to all following specimens.

4.3 | Specimen 4 × 4 × 32

The stress strain curves shown in Figure 9c show a similar tensile behaviour in the front and the back part with the back being slightly stronger. The back shows a lower fibre content than the front, but a better alignment of the fibres in the tensile direction, see Figure 14. Additionally, fibres are more homogeneously distributed over the sample height in the back part, see Figure 15.

Both specimens show a reduced fibre density in the upper part. The effect is more pronounced in the front than in the back. Orientations are very homogeneous over the complete height with no significant differences between front and back. The profiles in X-direction show

may partially be explained by a displacement of the fibres to the right due to the silica agglomeration (Figure 13, bottom left). It seems that this displacement also leads to the fibre misalignment towards the right edge of the specimen (Figure 13, bottom right).
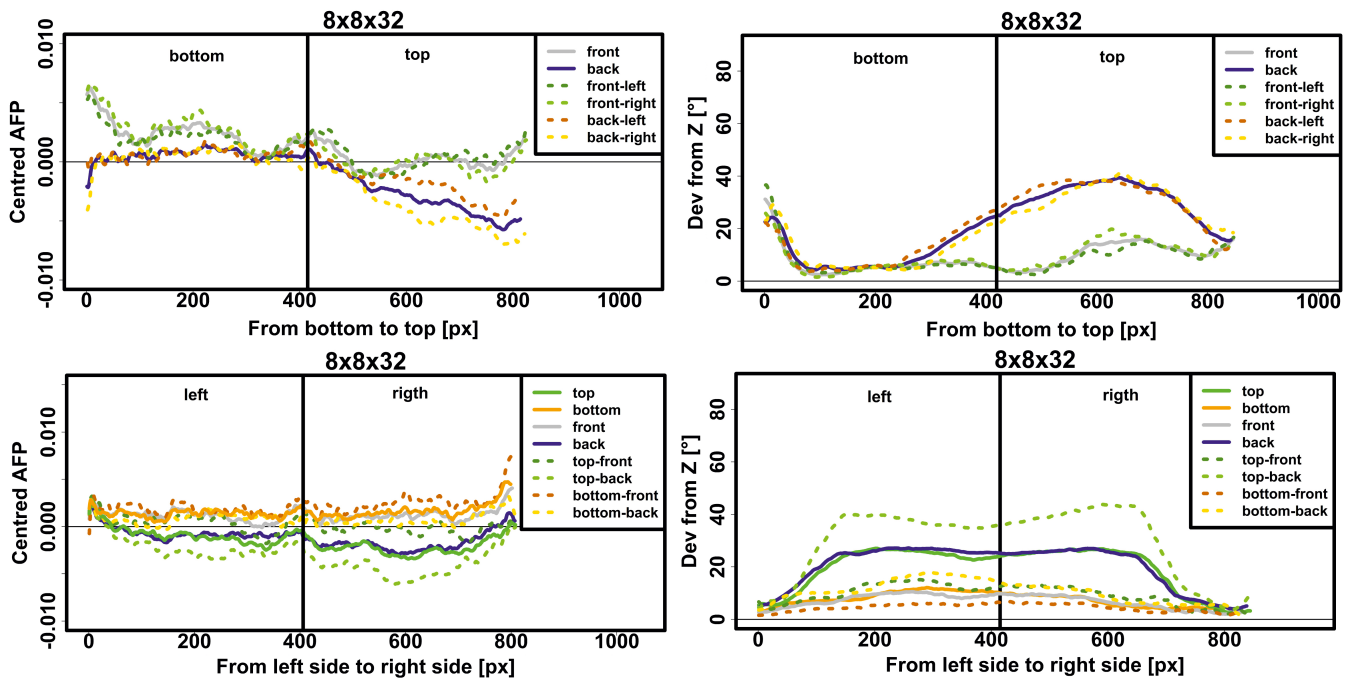
FIGURE 19 Specimen $8 \times 8 \times 32$: Centred AFP (left) and deviation of the fibre orientations from the Z-axis (right) along Y-direction (top) and along the X-direction (bottom)
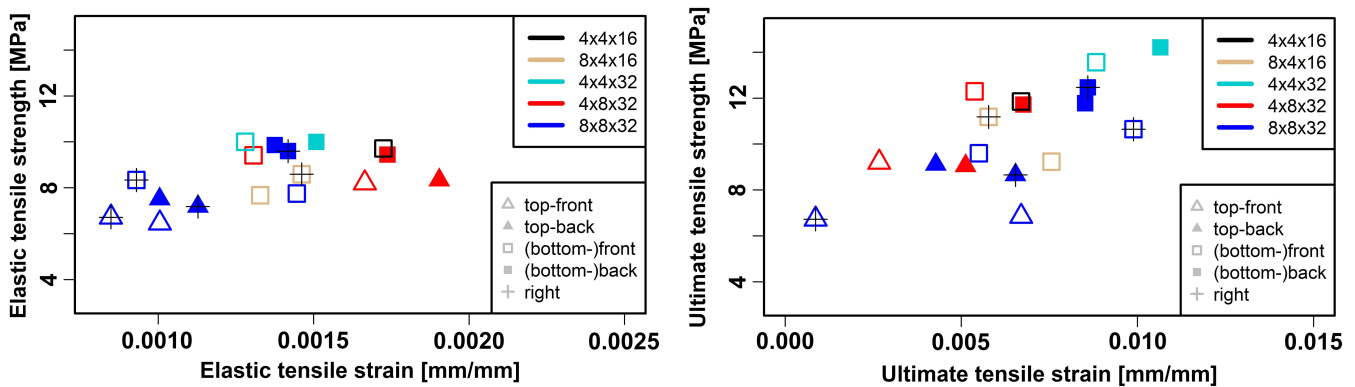

FIGURE 20 Correlations between elastic (left) and ultimate (right) stress and strain

a symmetric and very homogeneous structure both regarding fibre content and fibre orientation, see Figure 15.

4.4 | Specimen $4 \times 8 \times 32$

According to the stress strain curves, see Figure 9d, the two lower specimens are clearly stronger than the two upper ones. This observation can be explained by a reduced fibre density and poorer fibre alignment in the top part compared to the bottom, see Figures 16 and 17. There is no significant deviation between front and back parts. The fibre geometry is symmetric along its width.

4.5 | Specimen $8 \times 8 \times 32$

The stress strain curves for the eight subsamples of this specimen are shown in Figure 9e. In general, there are no significant differences between subsamples on the left and their counterparts on the right. In the remaining directions, the order from weakest to strongest is front top, back top, front bottom and back bottom. Hence, the subvolumes from the bottom are stronger than those from the top of the specimen. This can be explained by the lower fibre density and larger deviation from Z-axis in the top parts compared to the bottom, see Figures 18 and 19. Additionally, the back part is stronger than the front. The reason for this is less obvious. The volume rendering in the side view shown in Figure 18

shows a wavelike pattern with strong directional deviations in the front and in the upper back part. The trends in the curves are similar to those obtained for the $4 \times 8 \times 32$ specimen.

4.6 | Comparison of specimens

The calculated elastic and ultimate tensile strengths of the subspecimens and the corresponding strains are plotted in Figure 20. The elastic tensile strain ranges between 0.85 ‰ and 1.9 ‰ (mean value ∼1.3 ‰) and the ultimate tensile strain ranges between 2.6 ‰ and 10.65 ‰ (mean value approx. 6.5 ‰). As mentioned above, the results cannot be used to evaluate the size effect on the original specimens. They rather illustrate the influence of the specimen size on the local strength due to local variations in the fibre geometry. Figure 20 shows that the subspecimens in the top tend to have reduced elastic and ultimate strength compared to those in the bottom. In the same way, subspecimens from the front show a smaller strength than those from the back. The difference between the left and right subspecimens seems to be negligible. Subspecimens of specimen $4 \times 8 \times 32$ are stronger than the corresponding subspecimens of the enlarged specimen $8 \times 8 \times 32$. Subspecimens of the smaller specimens $4 \times 4 \times 16$ and $4 \times 4 \times 32$ show a higher strength than those from the large specimens.

5 | CONCLUSION

In this article, the influence of the specimen size on the fibre geometry in fine-grained UHPFRC blended with 2 Vol.% straight micro-fibres was investigated. Specimens were produced in five sizes and cut into subspecimens of equal size. The subspecimens were imaged by micro-computed tomography. The fibre system was characterised slice-wise by computing the local fibre content (AFP) and fibre alignment (deviation from the Z-axis). Correlations between the fibre geometry and the tensile strength of the subspecimens were investigated. The general finding is that the fibre geometry changes locally when increasing the specimen size. This change depends on the direction in which the sample is enlarged, i.e., increasing the width has a different effect than increasing the length or depth. The following conclusions can be drawn:

- Up to reflection, the fibre geometries in the left and the right subspecimen show the same behaviour. Hence, also the results of the tensile tests are similar for left and right subspecimens. An exception was specimen $8 \times 4 \times 16$ which contained an abnormally large silica fume agglomeration. In absence of such anomalies, increasing the width of the specimen will

most likely have a negligible influence, if the casting is performed over the whole specimen width.
- Wavelike patterns induced by the flow lines close to the casting point are more pronounced in higher and longer specimens. This resulted in a reduced tensile strength of the front subspecimens in specimens $4 \times 8 \times 32$ and $8 \times 8 \times 32$.
- For fixed cross-section size, increasing the specimen length gradually decreases the fibre content along the Z-axis. However, the alignment to the Z-axis improves.
- Edge effects of different magnitude were observed close to the sides and the bottom in all specimens.
- Local changes in the fibre geometry resulted in varying tensile strength of the subspecimens. Subspecimens showed an increased tensile strength in the bottom and back parts and a decreased tensile strength in the top and front parts. This is consistent with findings in References 31,32.
- Compared to the smallest specimen $4 \times 4 \times 16$, subspecimens of the larger specimens showed a slight reduction in the tensile strength.

In conclusion, changing the specimen size causes local changes in the fibre geometry which influences the tensile strength. Specimen height appears to be the most determining parameter followed by specimen length. Specimen width seems to be less important. For further investigation of the size effect on the flexural behaviour of UHPFRC, mechanical tests will be performed on a series of specimens of different sizes. These tests may also reveal to which extent the mechanical strength of a large specimen can be inferred from information on the subspecimens.

DATA AVAILABILITY STATEMENT
The data that support the findings of this study are available from the corresponding author upon reasonable request.

ORCID
Kasem Maryamh https://orcid.org/0000-0001-5630-8889
Konstantin Hauch https://orcid.org/0000-0002-2333-5191
Claudia Redenbach https://orcid.org/0000-0002-8030-069X

REFERENCES

1. Fehling E., Schmidt M., Teichmann T., Bunje K., Bornemann R., and Middendorf B. Entwicklung, Dauerhaftigkeit und Berechnung Ultrahochfester Betone (UHPC). Schriftenreihe Baustoffe und Massivbau, Heft Nr. 1. Kassel University Press GmbH, 2005.

2. Stürwald S. Rissentwicklung bei kombiniert bewehrten UHPC-Balken. 53. Forschungskolloquim DAfStb: Kassel University Press GmbH; 2008.

3. Leutbecher T. Rissbildung und Zugtragverhalten von mit Stabstahl und Fasern bewehrtem Ultrahochfesten Beton (UHPC). Kassel: Kassel University Press GmbH; 2008.

4. DAfStb-Heft 561. Sachstandsbericht Ultrahochfester Beton. Berlin: Beuth; 2008.

5. Fröhlich S, Schmidt M. Rheologische Eigenschaften von Faserhaltigem Ultrahochfesten Beton. 53. Forschungskolloquim DAfStb: Kassel University Press GmbH; 2008.

6. Maryamh K, Hauch K, Redenbach C, Schnell J. Influence of production parameters on the fiber geometry and the mechanical behavior of ultra high performance fiber-reinforced concrete. Struct Concr. 2021;22: 361–375.

7. Wille K, Parra-Montesinos GJ. Effect of beam size, casting method, and support condition on flexural behavior of ultra-high-performance fibre-reinforced concrete. ACI Mater. 2012; 109(3):379–388.

8. Kang S, Kim J. Numerical simulation of the variation of fiber orientation distribution during flow molding of ultra high performance cementitious composites (UHPCC). Cem Concr Compos. 2012;34(2):208–17.

9. Larsen IL, Thorstensen RT. The influence of steel fibres on compressive and tensile strength of ultra high performance concrete: A review. Construct Build Mater. 2020;256:119459.

10. Mahmud GH, Yang Z, Hassan AMT. Experimental and numerical studies of size effects of ultra high performance steel fibre reinforced concrete (uhpfrc) beams. Constr Build Mater. 2013; 48:1027–34.

11. Nguyen DL, Kim DJ, Ryu GS, Koh KT. Size effect on flexural behavior of ultra-highperformance hybrid fiber-reinforced concrete. Compos B: Eng. 2013;45(1):1104–16.

12. Sadegh K, Adam L. Influence of specimen size and fiber content on mechanical properties of ultra-high-performance fiber-reinforced concrete. ACI Mater J. 2012;109:675–84.

13. Fládr J, Bílý P. Specimen size effect on compressive and flexural strength of high-strength fibrereinforced concrete containing coarse aggregate. Compos B Eng. 2018;138:77–86.

14. Yoo D, Banthia N, Kang S, Yoon Y. Size effect in ultra-high-performance concrete beams. Eng Fract Mech. 2016;157: 86–106.

15. Weibull W. A statistical distribution function of wide applicability. J Appl Mech. 1951;18:293–7.

16. Bažant ZP. Size effect in blunt fracture: Concrete, rock, metal. J Eng Mech. 1984;110(4):518–35.

17. Bažant ZP, Kazemi M. Determination of fracture energy, process zone length and brittleness number from size effect, with application to rock and concrete. Int J Fract. 1990;44:111–31.

18. AFGC Recommendation. Recommendations: association francais de genie civil (AFGC). Documents scientifiques et technique; Ultra High Performance Firbre-Reinforced Concrete. 2013.

19. Department of Image Processing Fraunhofer Institute for Industrial Mathematics ITWM. MAVI: Modular Algorithms for Volume Images. Germany: Kaiserslautern. 2005.

20. Fraunhofer ITWM. ToolIP tool for image processing. itwm. fraunhofer.de/toolip, 2020.

21. Herman G.T. Correction for beam hardening in computed tomography. Phys Med Biol, 24(1):81–106, jan 1979.

22. Soille P. Morphological Image Analysis. Heidelberg: Springer-Verlag Berlin; 2004.

23. Otsu N. A threshold selection method from gray-level histograms. IEEE Trans Syst Man Cybern. 1979;9(1):62–6.

24. Danielsson P. Euclidean distance mapping. Comput Graph Image Process. 1980;14(3):227–48.

25. Chiu SN, Stoyan D, Kendall WS, Mecke J. Stochastic Geometry and its Applications. Wiley Series in Probability and Statistics. Chichester: Wiley; 2013.

26. Heckel F, Meine H, Moltz JH, et al. Segmentation-based partial volume correction for volume estimation of solid lesions in CT. IEEE Trans Med Imaging. 2014;33(2):462–80.

27. R Core Team. stats: R statistical functions. Vienna, Austria: R Foundation for Statistical Computing; 2019.

28. Pastorelli E, Herrmann H. Time-efficient automated analysis for fibre orientations in steel fibre reinforced concrete. Proc Eston Acad Sci. 2016;65:28–36.

29. Wirjadi O, Schladitz K, Easwaran P, Ohser J. Estimating fibre direction distributions of reinforced composites from tomographic images. Image Anal Stereol. 2016;35(3):167–79.

30. Fisher NI, Embleton BJJ, Lewis T. Statistical Analysis of Spherical Data. Cambridge: Cambridge University Press; 1987.

31. Herrmann H, Goidyk O, Naar H, Tuisk T, Braunbrück A. The influence of fiber orientation in self-compacting concrete on 4-point bending strength. Proc Eston Acad Sci. 2019;68:337–46.

32. Leutbecher T, Rebling J. Experimentelle Untersuchungen zur Ableitung der zentrischen Nachrisszugfestigkeit von UHFB aus Biegeversuchen. Bauingenieur. 2018;93(11):463–72.

AUTHOR BIOGRAPHIES
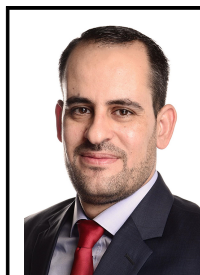
Kasem Maryamh, Faculty of Civil Engineering, Technische Universität Kaiserslautern, Institute of Concrete Structures and Structural Design, Kaiserslautern, Germany. Email: kasem.maryamh@bauing.uni-kl.de

Konstantin Hauch, Department of Mathematics, Technische Universität Kaiserslautern, Kaiserslautern, Germany. Email: hauch@mathematik.uni-kl.de

Claudia Redenbach, Department of Mathematics, Technische Universität Kaiserslautern, Kaiserslautern, Germany. Email: redenbach@mathematik.uni-kl.de

Jürgen Schnell, Faculty of Civil Engineering, Technische Universität Kaiserslautern, Institute of Concrete Structures and Structural Design, Kaiserslautern, Germany. Email: juergen.schnell@bauing.uni-kl.de

How to cite this article: Maryamh K, Hauch K, Redenbach C, Schnell J. Influence of specimen size on the fibre geometry and tensile strength of ultra-high-performance fibre-reinforced concrete. *Structural Concrete*. 2022;23:1239–1252. https://doi.org/10.1002/suco.202000753